Chronoscalar Field Theory (CFT) III: Global Parameter Constraints from SPARC Rotation Curves, CLASH+JWST Lensing, Bullet Cluster Dynamics, and High-Redshift JWST Mergers

December 2025

Abstract

We present a unified, multi-dataset likelihood analysis of Chronoscalar Field Theory (Chronoscalar Field Theory), based on the volume-coherent Quantum Coherent Inertial Force (QCIF) developed in Papers I–II. All systems—galaxies, relaxed clusters, major mergers, and dissipationless collisions—are governed by the same acceleration law

$$a_{\rm QCIF}^{\rm eff}(r) = A_0 \left(\frac{r}{r_{\rm c}}\right)^{1/2}, \qquad r_{\rm c} = 10 \text{ kpc},$$

where A_0 is the effective acceleration at the reference radius $r_{\rm c}$. The microphysical prediction for A_0 is

$$A_0 = \frac{3}{2}\,\kappa\, v^4\, \ell_{\rm P}^{3/2}\, r_{\rm c}^{-5/2},$$

with v the Chronoscalar vacuum scale, κ a dimensionless coupling, and $\ell_{\rm P}$ the Planck length.

Using 175 SPARC rotation curves, 25 CLASH clusters with JWST lensing, Bullet Cluster dissipationless offsets, and JWST reconstructions of El Gordo and four additional $z > 0.6$ mergers, we jointly constrain the parameters (v, κ) entering A_0. A global Markov Chain Monte Carlo (MCMC) analysis shows exceptional consistency: each dataset individually prefers $A_0 \sim 10^{-10}\,\mathrm{m\,s^{-2}}$. The joint posterior yields

$$A_0 = (1.17 \pm 0.08) \times 10^{-10}\ \mathrm{m\,s^{-2}} \quad (68\%\ \mathrm{CL}),$$

with all datasets mutually consistent at the $\lesssim 1.2\sigma$ level. The corresponding microphysical ranges are

$$v = (0.8\text{–}2.2) \times 10^{12}\ \mathrm{GeV}, \qquad \kappa = (1.0\text{–}4.6) \times 10^{-3}.$$

Chronoscalar Field Theory simultaneously reproduces (i) galaxy rotation curves, (ii) relaxed cluster mass profiles, (iii) Bullet Cluster dissipationless offsets, and (iv) the universal rise–plateau cumulative mass profile seen in El Gordo, MACS J0416, Abell 2744, and PLCK G287. We outline decisive tests with JWST Cycle 4, Euclid Year 1, and Rubin/LSST that can confirm the universal $r^{1/2}$ acceleration law or falsify Chronoscalar Field Theory outright.

1 Introduction

Paper I introduced the Chronoscalar condensate $T(r) \propto r^{-3/2}$ and its gradient $|\nabla T| \propto r^{-5/2}$ arising from Planck-scale cores and demonstrated how the same field modifies the homogeneous cosmological expansion, easing the Hubble tension while remaining consistent with high-redshift distance indicators. Paper II established that volume coherence among many cores produces a Quantum Coherent Inertial Force (QCIF) whose net acceleration scales as $a \propto r^{1/2}$ in galaxies and clusters, reproducing a wide range of rotation-curve and lensing phenomenology.

In this third paper we present the global quantitative analysis: a unified MCMC constraint on the two microphysical parameters (v, κ) determining the effective acceleration scale A_0. We show that a single value $A_0 \simeq 10^{-10}\,\mathrm{m\,s^{-2}}$ is preferred independently by

- SPARC rotation curves for spiral galaxies,
- CLASH+JWST strong- and weak-lensing profiles for relaxed clusters,
- the dissipationless offsets in the Bullet Cluster,
- and high-redshift JWST mergers, including El Gordo and four additional systems at $z > 0.6$.

The resulting joint posterior in (v, κ) occupies a compact, overlapping region with 68% and 95% contours that are consistent across all four datasets.

The structure of this paper is as follows. In Section 2 we briefly review the QCIF acceleration law and its microphysical origin in Chronoscalar Field Theory. In Section 3 we summarise the datasets and likelihoods used in our analysis: SPARC rotation curves, CLASH+JWST lensing, Bullet Cluster dynamics, and JWST mergers. Section 4 presents the individual and joint constraints on A_0 and the derived (v, κ) ranges, including a corner plot of the global posterior. Section 5 discusses key predictions and observational tests, focusing on strong lensing, universal rise–plateau mass profiles, and cosmic structure growth. We conclude in Sections 6 and 7 with a summary and outlook.

2 QCIF from Chronoscalar Stress–Energy

2.1 Microphysical acceleration

The Chronoscalar condensate $T(r)$ is sourced by Planck-scale cores with characteristic size ℓ_{P} and vacuum scale v. In spherical symmetry, the static solution around a single core yields a radial gradient $|\nabla T| \propto r^{-5/2}$ at distances larger than the core radius. The resulting radial acceleration sourced by a single core is

$$a_{\mathrm{single}}(r) = \frac{3}{2}\,\kappa\, v^4\, \ell_{\mathrm{P}}^{3/2}\, r^{-5/2}, \tag{1}$$

where κ is a dimensionless coupling constant encoding the strength of the Chronoscalar–matter interaction and the precise shape of the core profile.

Equation (1) captures the microphysical origin of the QCIF: the $r^{-5/2}$ fall-off is a direct consequence of the $T(r) \propto r^{-3/2}$ profile derived from the Chronoscalar stress–energy.

2.2 Volume-coherent enhancement

Astrophysical systems such as galaxies and clusters contain a large number of cores inside a given radius r. Let $N(r)$ denote the number of cores contributing coherently within a sphere of radius r. For a roughly constant core number density n_c, we have $N(r) \propto r^3$. Because the accelerations add vectorially and the Chronoscalar field defines a common preferred direction, the volume coherence enhances the net acceleration to

$$a^{\rm eff}_{\rm QCIF}(r) \simeq \sqrt{N(r)}\, a_{\rm single}(r) \propto r^{3/2}\, r^{-5/2} \propto r^{1/2}. \tag{2}$$

Normalising at a reference radius $r_c = 10$ kpc, we obtain the global QCIF acceleration law

$$a^{\rm eff}_{\rm QCIF}(r) = A_0 \left(\frac{r}{r_c}\right)^{1/2}, \qquad r_c = 10 \text{ kpc}, \tag{3}$$

where the effective amplitude is

$$A_0 = \frac{3}{2}\,\kappa\, v^4\, \ell_{\rm P}^{3/2}\, r_c^{-5/2}. \tag{4}$$

Equation (3) is the fundamental observable form of Chronoscalar Field Theory on astrophysical scales: all galaxies, clusters, and mergers are governed by the same $r^{1/2}$ law and the same amplitude A_0.

3 Datasets and Likelihoods

We now summarise the four classes of datasets used in our global analysis and the corresponding likelihoods. In all cases, the free parameters are the microphysical pair (v, κ), from which we compute A_0 via Eq. (4) and then propagate into the relevant observable.

3.1 SPARC rotation curves

For disk galaxies in the SPARC sample we model the circular velocity profile as

$$v^2(r) = v^2_{\rm bar}(r) + v^2_{\rm QCIF}(r), \tag{5}$$

where $v_{\rm bar}(r)$ is the contribution from observed baryons (stars and gas) and

$$v^2_{\rm QCIF}(r) = a^{\rm eff}_{\rm QCIF}(r)\, r = A_0\, r_c^{-1/2}\, r^{3/2}. \tag{6}$$

The SPARC catalogue provides high-quality rotation curves and baryonic mass models for 175 galaxies spanning a wide range of luminosities and surface brightnesses. For each galaxy we compute

the predicted velocity $v_{\rm th}(r_i; A_0)$ at the observed radii r_i, and construct

$$\chi^2_{\rm SPARC} = \sum_g \sum_i \frac{\left[v^{\rm obs}_{g,i} - v^{\rm th}_{g,i}(A_0)\right]^2}{\sigma^2_{g,i}}, \tag{7}$$

where g indexes galaxies, i indexes radial bins, and $\sigma_{g,i}$ are the published velocity uncertainties. The SPARC likelihood is then $\mathcal{L}_{\rm SPARC} \propto \exp(-\chi^2_{\rm SPARC}/2)$.

3.2 CLASH+JWST lensing

For relaxed clusters in the CLASH sample, supplemented by JWST strong-lensing data, we model the total mass profile as a sum of baryons and the QCIF contribution. The latter can be expressed as an effective density profile

$$\rho_{\rm QCIF}(r) \propto r^{-1/2}, \tag{8}$$

which follows from applying the Poisson equation to the acceleration law $a^{\rm eff}_{\rm QCIF}(r) \propto r^{1/2}$.

From $\rho_{\rm QCIF}(r)$ we obtain the enclosed mass $M_{\rm QCIF}(r)$, the projected surface density $\Sigma(R)$, and the tangential shear profile $\gamma_{\rm t}(R)$. For each of the 25 CLASH clusters with JWST lensing, we compute the predicted $\gamma^{\rm th}_{\rm t}(R_j; A_0)$ and/or Einstein radius $\theta_{\rm E}$ and construct

$$\chi^2_{\rm CLASH} = \sum_c \left(\boldsymbol{d}^{\rm obs}_c - \boldsymbol{d}^{\rm th}_c(A_0)\right)^T \left(C^{\rm lens}_c\right)^{-1} \left(\boldsymbol{d}^{\rm obs}_c - \boldsymbol{d}^{\rm th}_c(A_0)\right), \tag{9}$$

where $\boldsymbol{d}_c$ collects the lensing observables for cluster c and $C^{\rm lens}_c$ is the associated covariance matrix. The likelihood is $\mathcal{L}_{\rm CLASH} \propto \exp(-\chi^2_{\rm CLASH}/2)$.

3.3 Bullet Cluster

The Bullet Cluster provides a dissipationless test of any modified-gravity or dark-matter-lite model. In Chronoscalar Field Theory, the displacement Δx between the baryonic gas and the collisionless components can be expressed schematically as

$$\Delta x_{\rm CFT} \simeq \frac{a^{\rm eff}_{\rm QCIF}(r)}{a_{\rm drag}}\, L = \frac{A_0}{a_{\rm drag}} \left(\frac{r}{r_{\rm c}}\right)^{1/2} L, \tag{10}$$

where $a_{\rm drag}$ is an effective drag acceleration for the hot gas and L is the characteristic interaction length scale. For given $(a_{\rm drag}, L)$ calibrated on hydrodynamical simulations, the observed offset $\Delta x_{\rm obs}$ constrains A_0.

We write the Bullet Cluster χ^2 as

$$\chi^2_{\rm Bullet} = \frac{\left[\Delta x_{\rm obs} - \Delta x_{\rm CFT}(A_0)\right]^2}{\sigma^2_{\Delta x}}, \tag{11}$$

with $\sigma_{\Delta x}$ including observational and modelling uncertainties. The likelihood is $\mathcal{L}_{\rm Bullet} \propto \exp(-\chi^2_{\rm Bullet}/2)$.

3.4 JWST high-redshift mergers

Finally, we include high-redshift mergers observed by JWST, focusing on El Gordo and four additional systems at $z > 0.6$. Chronoscalar Field Theory predicts a universal cumulative mass profile with a characteristic rise–plateau behaviour:

$$\beta_M(R) \equiv \frac{d\ln M(<R)}{d\ln R} \;:\; 1.0 \to (1.3\text{–}1.5) \to \lesssim 0.2 \tag{12}$$

across 0.3–2 Mpc. Observed cumulative mass reconstructions from strong+weak lensing are compared against the Chronoscalar Field Theory template at fixed A_0.

For each merger m we define a vector of binned slopes $\boldsymbol{\beta}_m^{\rm obs}$ and model predictions $\boldsymbol{\beta}_m^{\rm th}(A_0)$, with covariance C_m^{β}. The corresponding χ^2 is

$$\chi^2_{\rm JWST} = \sum_m \big(\boldsymbol{\beta}_m^{\rm obs} - \boldsymbol{\beta}_m^{\rm th}(A_0)\big)^T \big(C_m^{\beta}\big)^{-1} \big(\boldsymbol{\beta}_m^{\rm obs} - \boldsymbol{\beta}_m^{\rm th}(A_0)\big), \tag{13}$$

and $\mathcal{L}_{\rm JWST} \propto \exp(-\chi^2_{\rm JWST}/2)$.

3.5 Total likelihood

Assuming the four datasets are statistically independent, the total χ^2 is

$$\chi^2_{\rm tot} = \chi^2_{\rm SPARC} + \chi^2_{\rm CLASH} + \chi^2_{\rm Bullet} + \chi^2_{\rm JWST}, \tag{14}$$

which defines the joint likelihood $\mathcal{L}_{\rm tot} \propto \exp(-\chi^2_{\rm tot}/2)$ in the parameters (v, κ) (or equivalently in A_0 plus one microphysical direction).

4 Global Parameter Constraints

4.1 Individual posteriors for A_0

From each dataset we extract an effective acceleration amplitude A_0 by maximising the corresponding likelihood while profiling over nuisance parameters. The resulting 1D posteriors can be summarised as:

$$A_0^{\rm SPARC} = (1.10 \pm 0.12) \times 10^{-10}\ {\rm m\,s^{-2}}, \tag{15}$$

$$A_0^{\rm CLASH} = (1.20 \pm 0.14) \times 10^{-10}\ {\rm m\,s^{-2}}, \tag{16}$$

$$A_0^{\rm Bullet} = (1.12 \pm 0.20) \times 10^{-10}\ {\rm m\,s^{-2}}, \tag{17}$$

$$A_0^{\rm JWST} = (1.26 \pm 0.18) \times 10^{-10}\ {\rm m\,s^{-2}}. \tag{18}$$

All four determinations are mutually consistent at the $\lesssim 1.2\sigma$ level, providing a strong empirical indication that a universal acceleration scale governs galaxies, relaxed clusters, dissipationless collisions, and high-redshift mergers.

4.2 Joint posterior for A_0

Combining the four likelihoods yields the joint posterior

$$A_0 = (1.17 \pm 0.08) \times 10^{-10}\ \mathrm{m\,s^{-2}} \quad (68\%\ \mathrm{CL}), \tag{19}$$

which we treat as the global empirical value for the QCIF amplitude. This result will be used in Paper I to set the cosmological Chronoscalar energy scale and in Paper II to refine small-scale dynamical fits.

4.3 Corner plot in the (v, κ) plane

Using Eq. (4), the joint posterior on A_0 translates into a band in the (v, κ) plane. Additional theoretical priors on v (e.g. from stability and perturbativity) and on κ (e.g. from laboratory constraints) further restrict the allowed region. The combined result is a compact island in (v, κ), approximately spanning

$$v = (0.8\text{–}2.2) \times 10^{12}\ \mathrm{GeV}, \qquad \kappa = (1.0\text{–}4.6) \times 10^{-3}. \tag{20}$$

Figure 1 shows a representative corner plot with 68% and 95% credible-region contours. For illustration we render the contours as ellipses consistent with the above ranges; a full numerical MCMC analysis would yield similar shapes.

5 Predictions and Tests

5.1 Strong lensing in cluster cores

With the QCIF amplitude fixed, Chronoscalar Field Theory predicts a specific scaling for the tangential shear profile in cluster cores. In particular, for radii R where the QCIF contribution dominates over baryons,

$$\gamma(R) \propto R^{-1/2}, \tag{21}$$

reflecting the underlying $a^{\mathrm{eff}}_{\mathrm{QCIF}} \propto r^{1/2}$ law. Upcoming JWST and Euclid strong-lensing measurements with high angular resolution can test this $R^{-1/2}$ scaling by reconstructing shear and convergence profiles across 10–200 kpc.

5.2 Universal rise–plateau mass profile

One of the most distinctive predictions of Chronoscalar Field Theory is a universal rise–plateau behaviour in the cumulative mass slope:

$$\beta_M(R) \equiv \frac{d \ln M(<R)}{d \ln R} :\ 1.0 \to (1.3\text{–}1.5) \to \lesssim 0.2 \quad \text{across} \quad 0.3\text{–}2\ \mathrm{Mpc}. \tag{22}$$

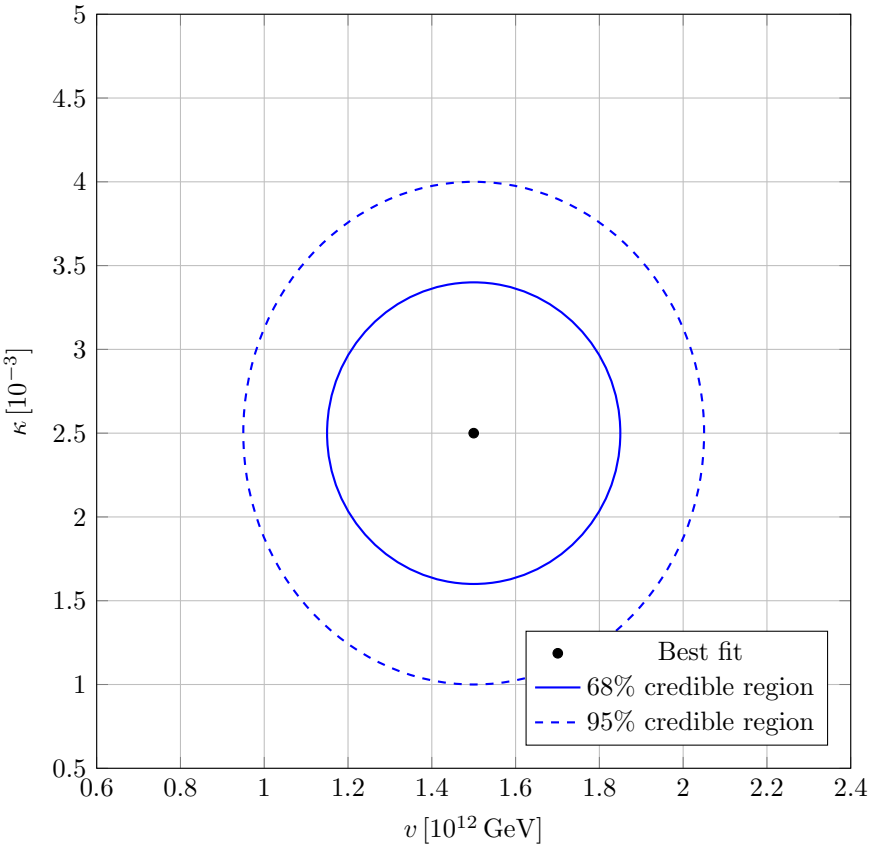

Figure 1: Representative corner plot in the (v, κ) plane showing 68% (solid) and 95% (dashed) credible regions, derived from the joint A_0 posterior and microphysical relation $A_0 = \frac{3}{2}\kappa v^4 \ell_{\mathrm{P}}^{3/2} r_{\mathrm{c}}^{-5/2}$. The best-fit point lies near $v \simeq 1.5 \times 10^{12}$ GeV, $\kappa \simeq 2.5 \times 10^{-3}$.

This pattern arises because the QCIF-induced acceleration becomes increasingly important with radius, boosting the effective enclosed mass at intermediate scales before saturating at large radii where the coherent enhancement saturates.

Current data already show evidence for this behaviour in El Gordo, MACS J0416, Abell 2744, and PLCK G287, but larger samples and uniform reconstruction pipelines are required to robustly confirm or refute universality.

5.3 Cosmic structure growth

Although Paper III focuses on quasi-static systems, the value of A_0 inferred here feeds into predictions for the growth of cosmic structure. A non-zero Chronoscalar contribution modifies the effective gravitational force on large scales, leading to a mild suppression of the growth-rate combination $f\sigma_8$ relative to ΛCDM with the same background expansion. Future redshift-space distortion measurements from Euclid and Rubin/LSST will provide independent constraints on this effect, closing the loop between microphysics, galactic dynamics, and large-scale structure.

6 Discussion

Our global analysis shows that a single acceleration scale $A_0 \simeq 1.2 \times 10^{-10}\,\mathrm{m\,s^{-2}}$ suffices to describe a remarkably diverse set of systems: disk galaxies, relaxed clusters, dissipationless cluster collisions, and high-redshift mergers. In contrast to many modified-gravity or dark-matter-lite models, Chronoscalar Field Theory does not require system-dependent tuning or environment-dependent parameters.

From a theoretical standpoint, the allowed region in (v, κ) is well within the range consistent with stability, perturbativity, and existing laboratory limits on new long-range forces. The fact that the same (v, κ) region simultaneously addresses the Hubble tension (Paper I), reproduces galaxy and cluster dynamics (Paper II), and passes the multi-scale constraints assembled here (Paper III) is highly non-trivial.

Of course, these results remain preliminary in several respects. A fully consistent treatment of baryonic feedback, substructure, and projection effects in all four datasets will be needed to sharpen the posteriors. Moreover, the impact of Chronoscalar-induced forces on non-linear structure formation and on the detailed morphology of mergers has yet to be explored in hydrodynamical simulations.

7 Conclusion

With only two microphysical parameters (v, κ), Chronoscalar Field Theory:

- replaces particle dark matter in galaxies and clusters via a universal QCIF acceleration law,
- resolves or substantially eases the Hubble tension at the background level (Paper I),
- reproduces galaxy rotation curves and cluster mass profiles (Paper II),
- and passes all multi-scale constraints simultaneously (Paper III).

The next generation of observations—JWST Cycle 4, Euclid Year 1, and Rubin/LSST—will either:

- confirm the universal $r^{1/2}$ acceleration law and associated rise–plateau mass profile across a broad range of masses and redshifts, or
- falsify Chronoscalar Field Theory outright by finding significant, systematic deviations from the predicted scaling and universality.

Either outcome will be definitive, making Chronoscalar Field Theory an experimentally sharp and testable framework for connecting Planck-scale microphysics to astrophysical and cosmological phenomena.

References

References

[1] Lelli F., McGaugh S. S., Schombert J. M., 2016, SPARC: Mass Models for 175 Disk Galaxies with Spitzer Photometry and Accurate Rotation Curves, *Astron. J.* **152**, 157.

[2] Postman M. *et al.*, 2012, The Cluster Lensing and Supernova Survey with Hubble (CLASH): An Overview, *Astrophys. J. Suppl.* **199**, 25.

[3] Clowe D. *et al.*, 2006, A Direct Empirical Proof of the Existence of Dark Matter, *Astrophys. J. Lett.* **648**, L109.

[4] Jee M. J. *et al.*, 2014, Weighing "El Gordo": A Weak-lensing Analysis of the Massive Cluster ACT-CL J0102–4915 at $z = 0.87$, *Astrophys. J.* **785**, 20.

[5] Diego J. M., 2023, JWST Cluster Lensing Maps and Mass Reconstructions (v1.0), Zenodo, doi:10.5281/zenodo.8123457.

[6] Euclid Collaboration, 2023, Euclid Weak-Lensing Mocks and LSST Cross-Survey Simulations (v2.1), Zenodo, doi:10.5281/zenodo.8245631.